Supporting information

Porous $NaTi_2(PO_4)_3$ nanocubes: high-rate nonaqueous sodium anode material with more than 10000 cycle life

Gongzheng Yang,[†,#] Huawei Song,[†,#] Mingmei Wu[§] and Chengxin Wang*[, †,‡,#]

[†]*The Key Laboratory of Low-Carbon Chemistry & Energy Conservation of Guangdong Province,* [‡]*State Key Laboratory of Optoelectronic Materials and Technologies,* [#]*School of Physics Science and Engineering,* [§]School of Chemistry and Chemical Engineering, *Sun Yat-sen (Zhongshan) University, Guangzhou 510275, People's Republic of China*

*Correspondence and requests for materials should be addressed to C. X. Wang.

Tel & Fax: +86-20-84113901

E-mail: wchengx@mail.sysu.edu.cn

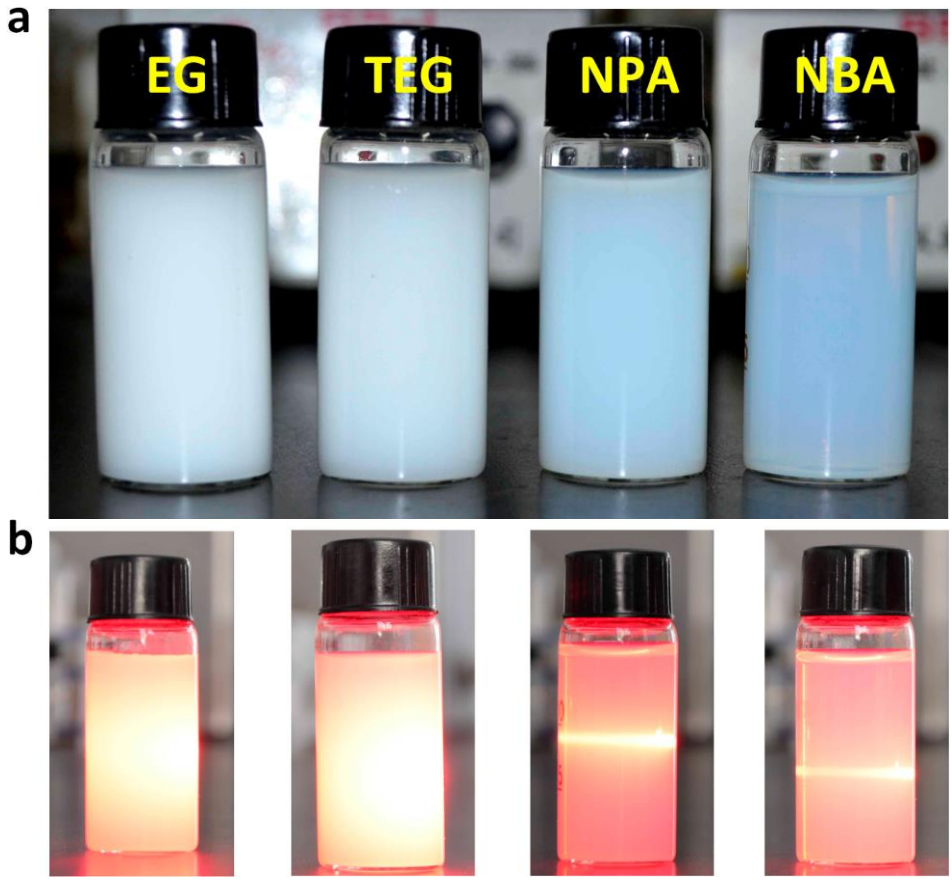

Figure S1. (a) Digital photos of the four NTP nanocubes that are dispersed in waters (concentrations of the dispersions are 3 mg mL^{-1}). (b) Digital photos illustrate the different optical phenomena as exposed by a beam of red light.

As shown in Figure S1a, the four NTP nanocubes have been ultrasonic dispersed in the waters with a same concentration. We can clearly see that all the products suspend evenly in the solutions, while the NTP-NPA and -NBA look much more transparent. In particularly, none of the nanoparticles precipitations of the NTP-NPA and -NBA can be observed even after standing for one week. Figure S1b present the digital photos of the different optical phenomena of the four NTP nanocubes as exposed by a beam of red light, in which the NTP-NPA and -NBA have apparently demonstrated the Tyndall effect, indicating their colloidal-like properties.

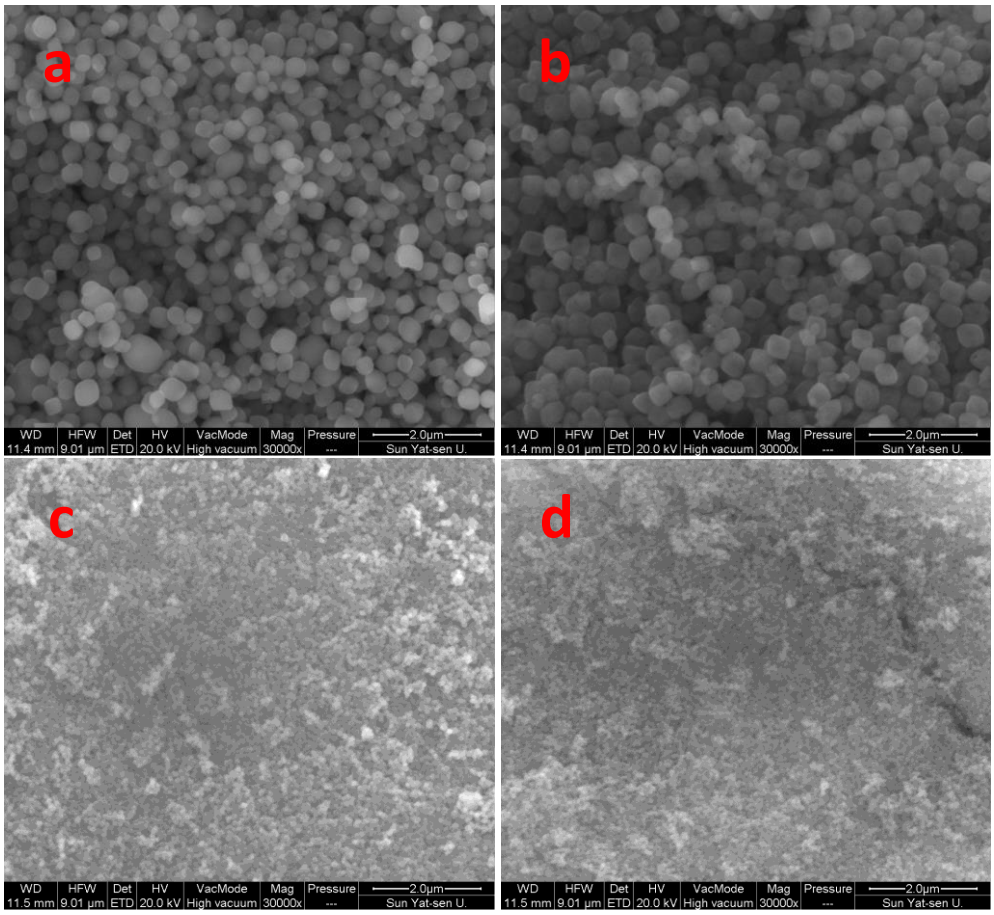

Figure S2. Low-magnification FESEM images of the NTP samples synthesized at different organic precursors: (a) EG; (b) TEG; (c) NPA; (d) NBA.

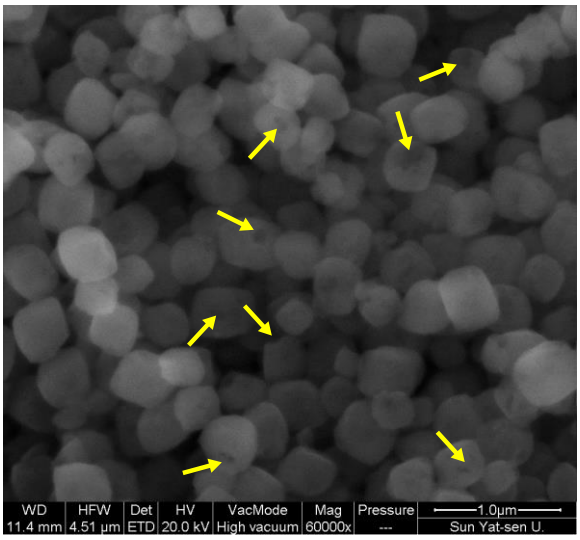

Figure S3. A high-magnification FESEM image of the samples NTP-TEG (the regions marked with yellow arrows show the cavities that embedded in the nanoparticles).

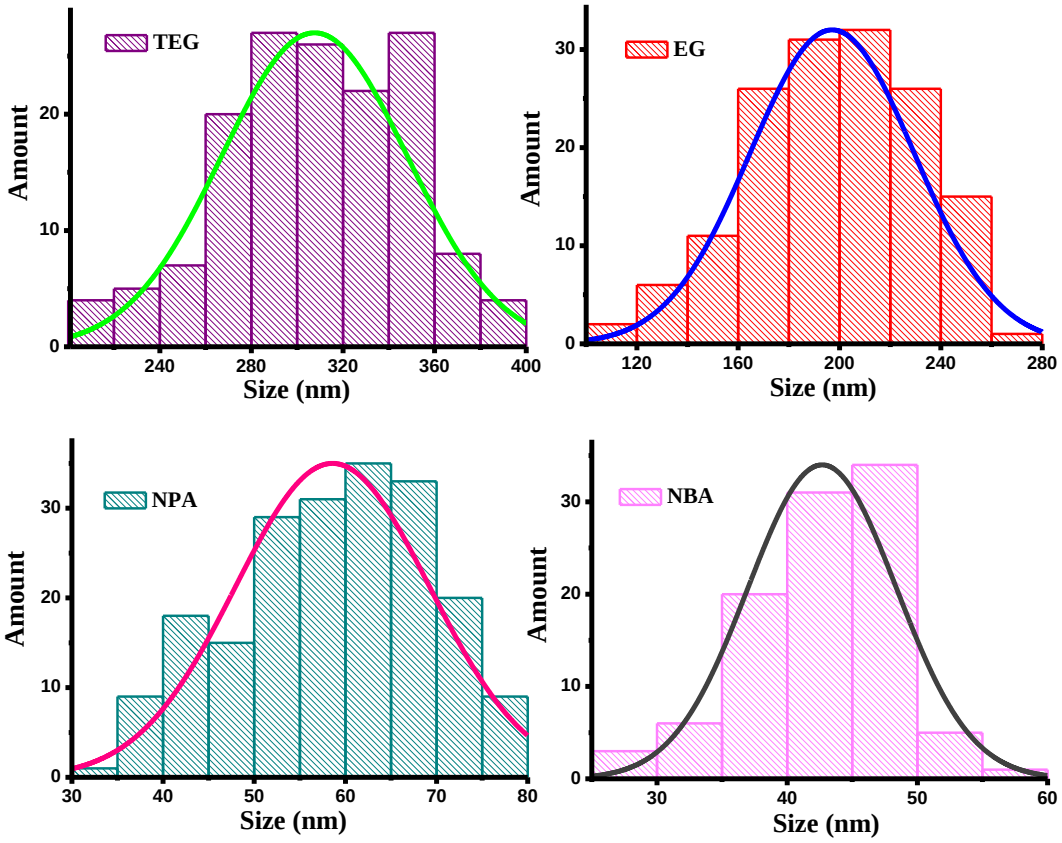

Figure S4. The grain sizes statistics of the four NTP nanoparticles.

Table S1. The average grain size and size distribution statistics of the products.

	NTP–EG	NTP–TEG	NTP–NPA	NTP–NBA
Size distribution (nm)	200 ~ 400	100 ~ 280	30 ~ 80	20 ~ 60
Average size (nm) TEM observation	307.5	197	58.6	42.7
Sizes (nm) Scherrer equation	40.0	12.6	43.1	40.6

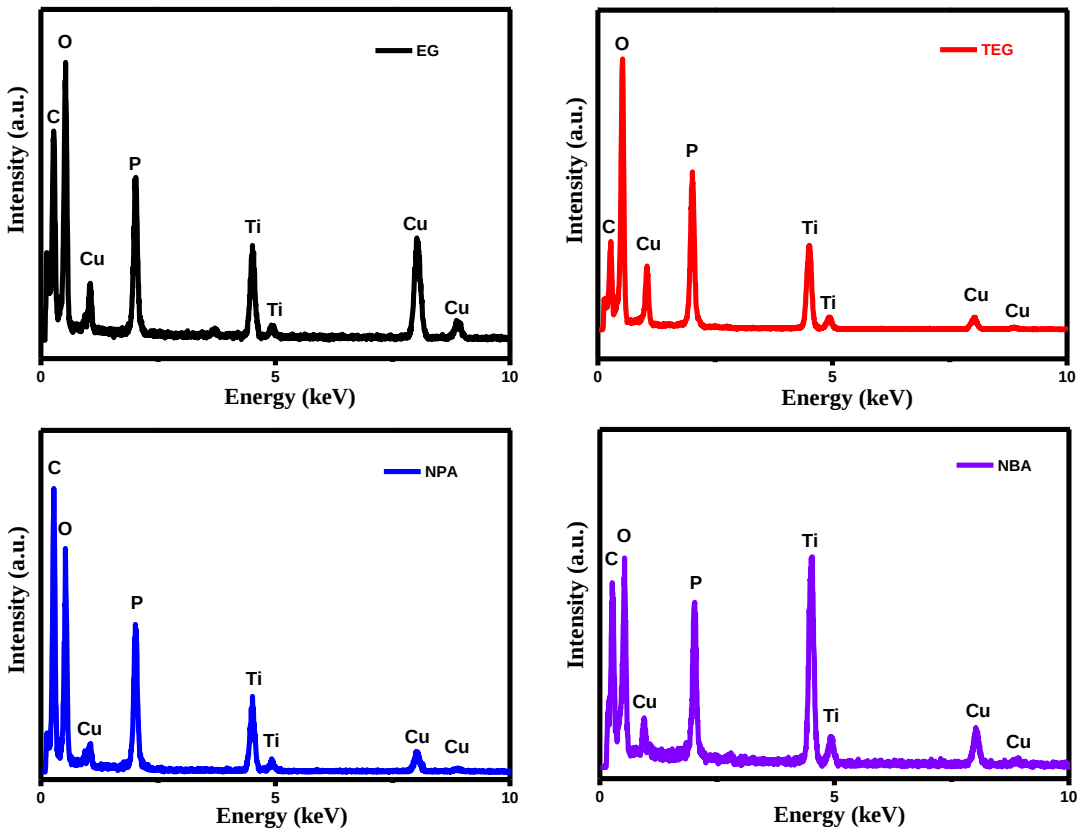

Figure S5. EDS patterns of the four NTP nanoparticles demonstrate the high purity of the products.

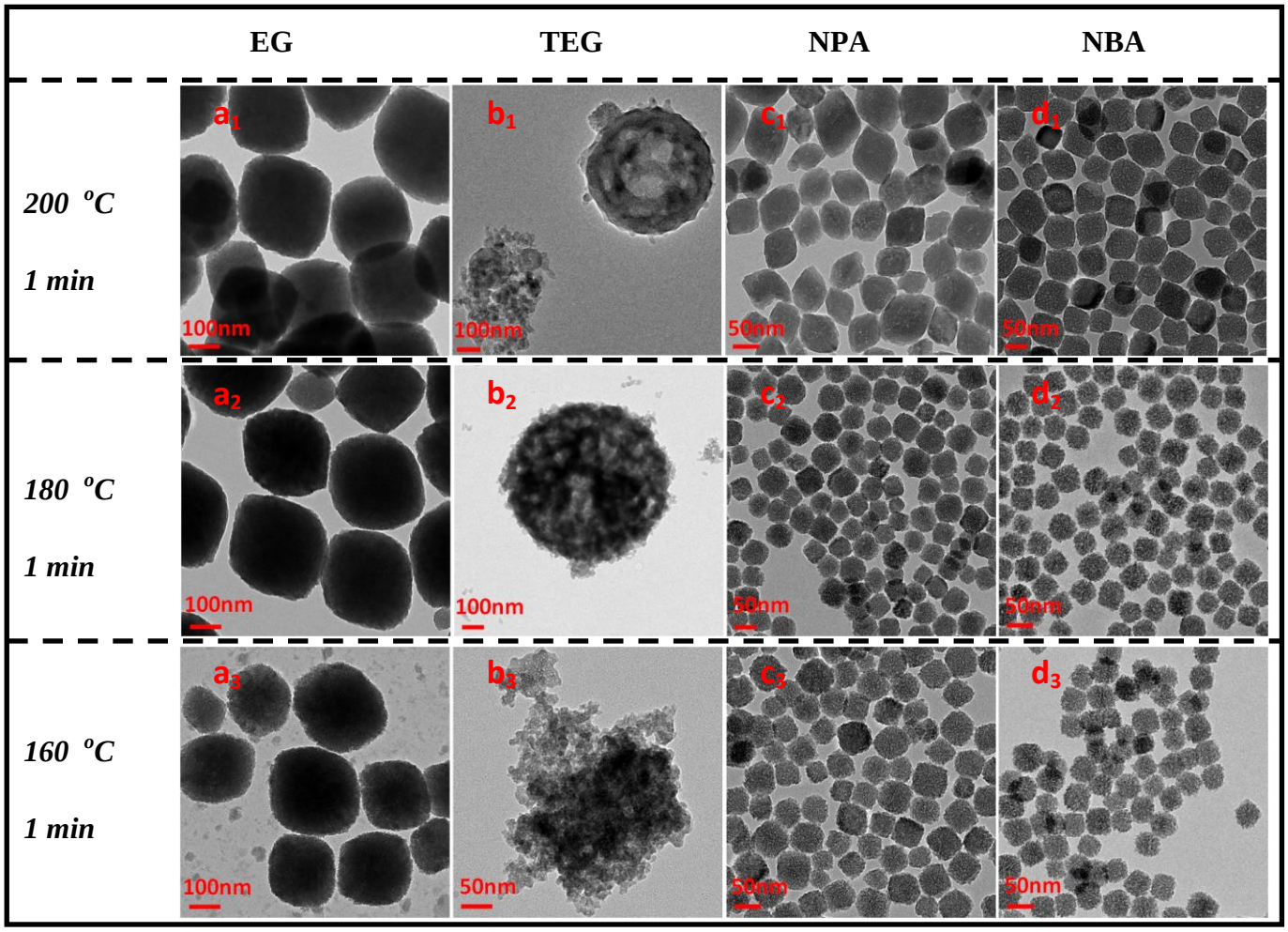

Figure S6. Typical TEM images of the products obtained at various stages: (a) NTP-EG; (b) NTP-TEG; (c) NTP-NPA; (d) NTP-NBA.

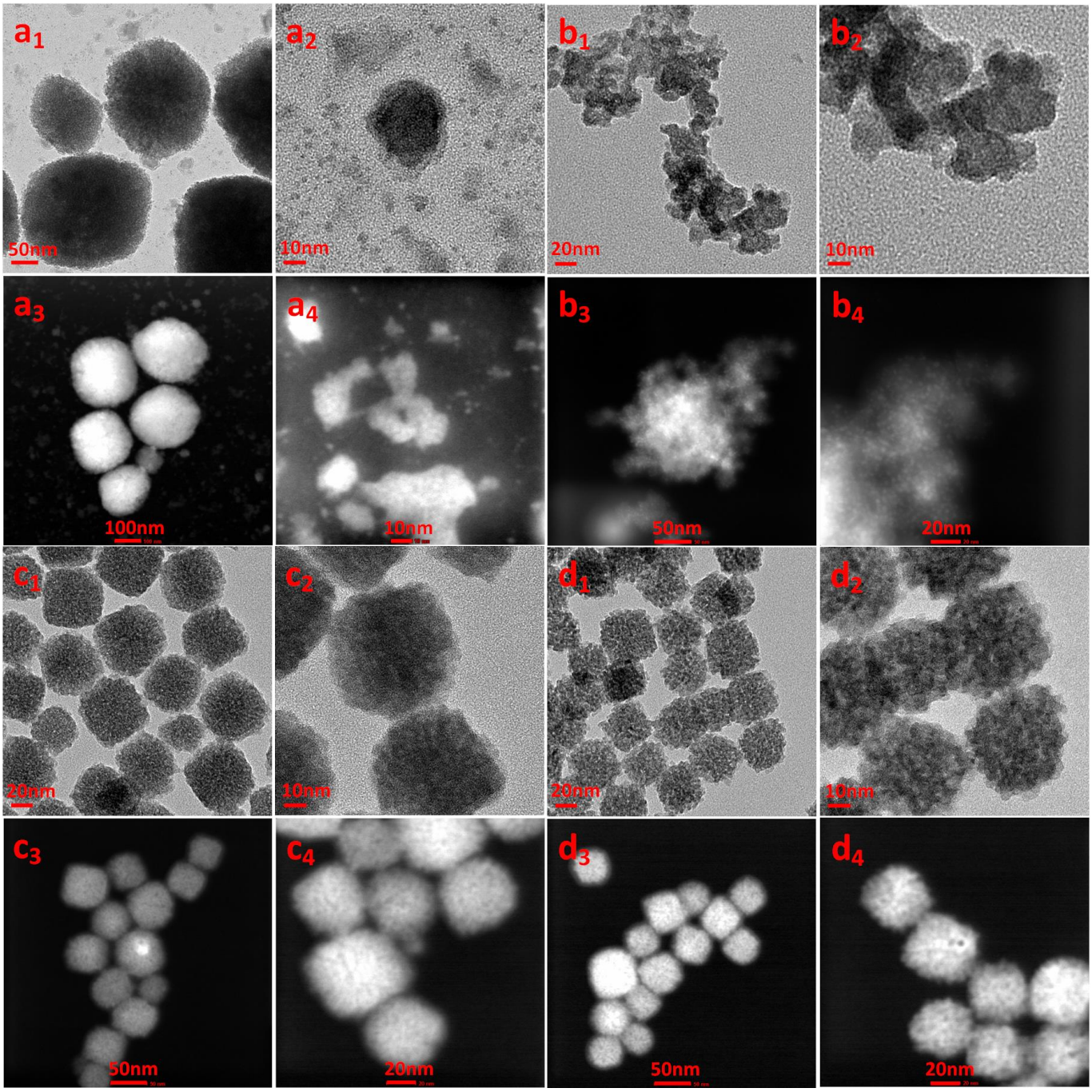

Figure S7. TEM and STEM images of the (a) NTP-EG, (b) NTP-TEG, (c) NTP-NPA and (d) NTP-NBA products collected at 160 ^{o}C for 1 min.

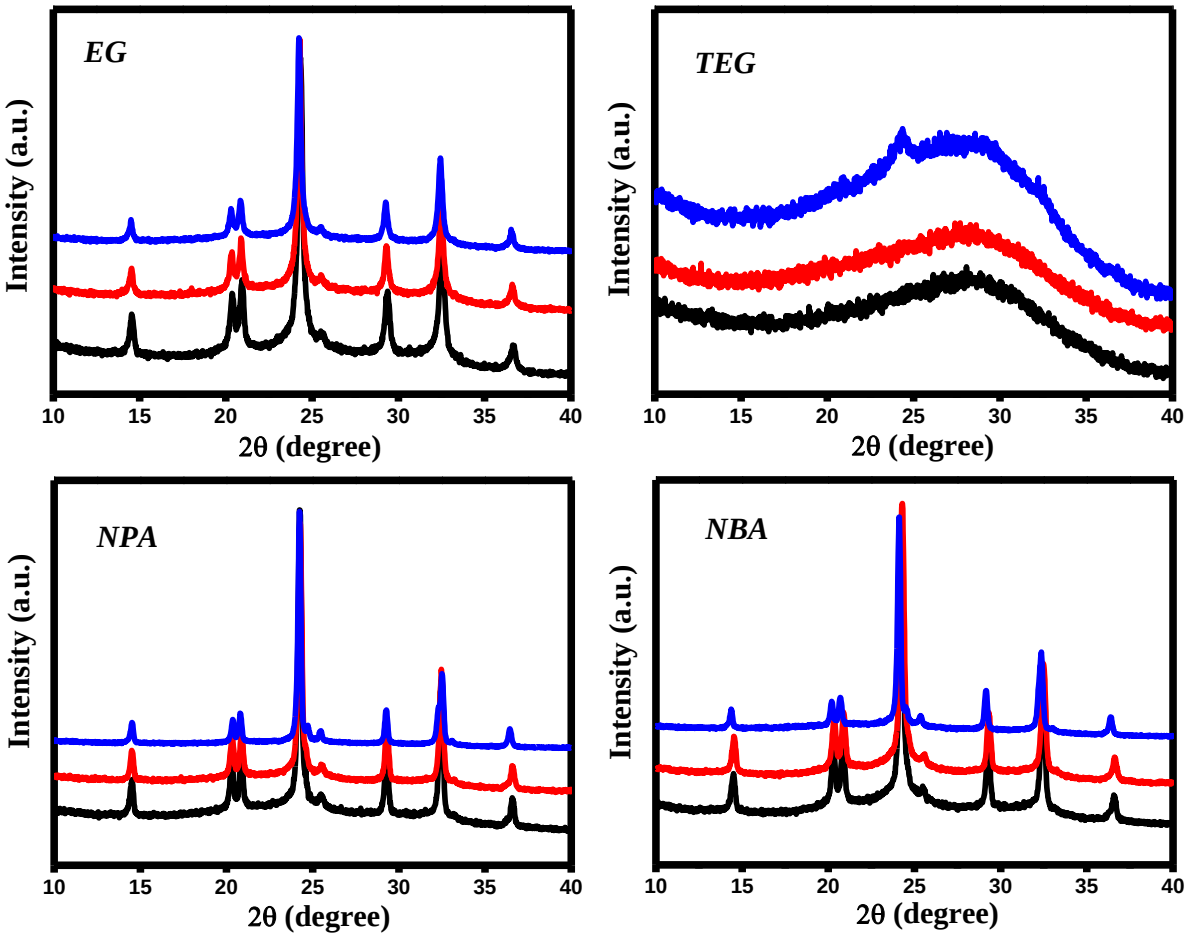

Figure S8. XRD patterns of the as-prepared four samples collected at different stages. Black line: 160 ^{o}C, 1 min; Red line: 180 ^{o}C, 1 min; Blue line: 200 ^{o}C, 1 min.

To understand the growth mechanism of these nanocubes, both temperature and time-dependent experiments were carried out. As shown in Figure S6, the samples collected at different stages present totally different morphologies. For the NTP-EG, the samples synthesized at 200 ^{o}C (Figure S6-a1) and 180 ^{o}C (Figure S6-a2) give the similar morphologies with the final products (Figure 1b), while considerable nanoparticles appear at 160 ^{o}C (Figure S6-a3). For the NTP-NPA (Figure S6c) and -NBA (Figure S6d), all the obtained nanocrystals demonstrate the same overall frameworks. However, by careful observations, one can see that the number of the mesopores gradually diminishes as decreasing the reaction temperature. Interestingly, a completely different morphology of NTP-TEG (Figure S6-b1) appears as merely reducing the reaction time from 1 h (Figure 1c) to 1 min, where the samples are consist of few porous spherical particles and lots of irregular nanoparticles. Until lowering the reaction temperature to 160 ^{o}C, there are only the irregular nanoparticles that can be found in the collected white powders (Figure S6-b3).

Now we have noticed that the morphological evolutions of the four NTP nanocubes primarily start from 160 ^{o}C, and consequently more studies on the samples collected at 160 ^{o}C were further conducted by TEM and STEM analyses. For the NTP-EG and -TEG, the STEM images in Figure S7-x3 and x4 (x = a, b) have clearly demonstrated that all the nanocubes and nanoparticles are constructed by the stacking of lots of quantum dots. Figure S7-c and d exhibit corresponding TEM and STEM images of the NTP-NPA and -NBA, in which one can see that all the nanocubes are made up of numerous tiny units, accompanying by the emergence of mesopores-like cavities among the stacking blocks.

XRD patterns of these products obtained at various stages are depicted in Figure S8. Apparently, all intensive peaks of the NTP- EG, -NPA and -NBA can be well indexed to R-3c diffraction pattern of $NaTi_2(PO_4)_3$, further implying that the final nanocubes are formed from the adjacent nanocrytals through atomically matched bond formation between specific facets. However, the XRD results collected from NTP-TEG show three sets of broad diffraction patterns where only two weak peaks can be observed from the samples synthesized at 200 ^{o}C, which are probably attributed to ultrafine nature of the constituent monomers (Figure S7-b4).

Thus, based upon the above observations, it is reasonable to speculate that all the NTP nanocubes are assembled from the tight aggregations of considerable building blocks of several distinct shapes via the different arrangements, namely the possible oriented-attachment growth mechanism. Furthermore, we have calculated the particle sizes of the building blocks of the four porous NTP nanocubes using Scherrer equation (based on the {102} facets, d = 0.61 nm) and corresponding results are illustrated in the table S1. It can be seen that the particle sizes are universally smaller than that collected from the low-magnification TEM observations (Fig. 1b-d), especially for the samples NTP–EG and –TEG. Moreover, interestingly, upon inspection of HRTEM and STEM tests, the particle sizes calculated using Scherrer equation show good agreement with the tiny units of these four NTP nanocubes . Thus, we can known the primary particle sizes of the samples which further confirms the possible architectures of the NTP nanocubes.

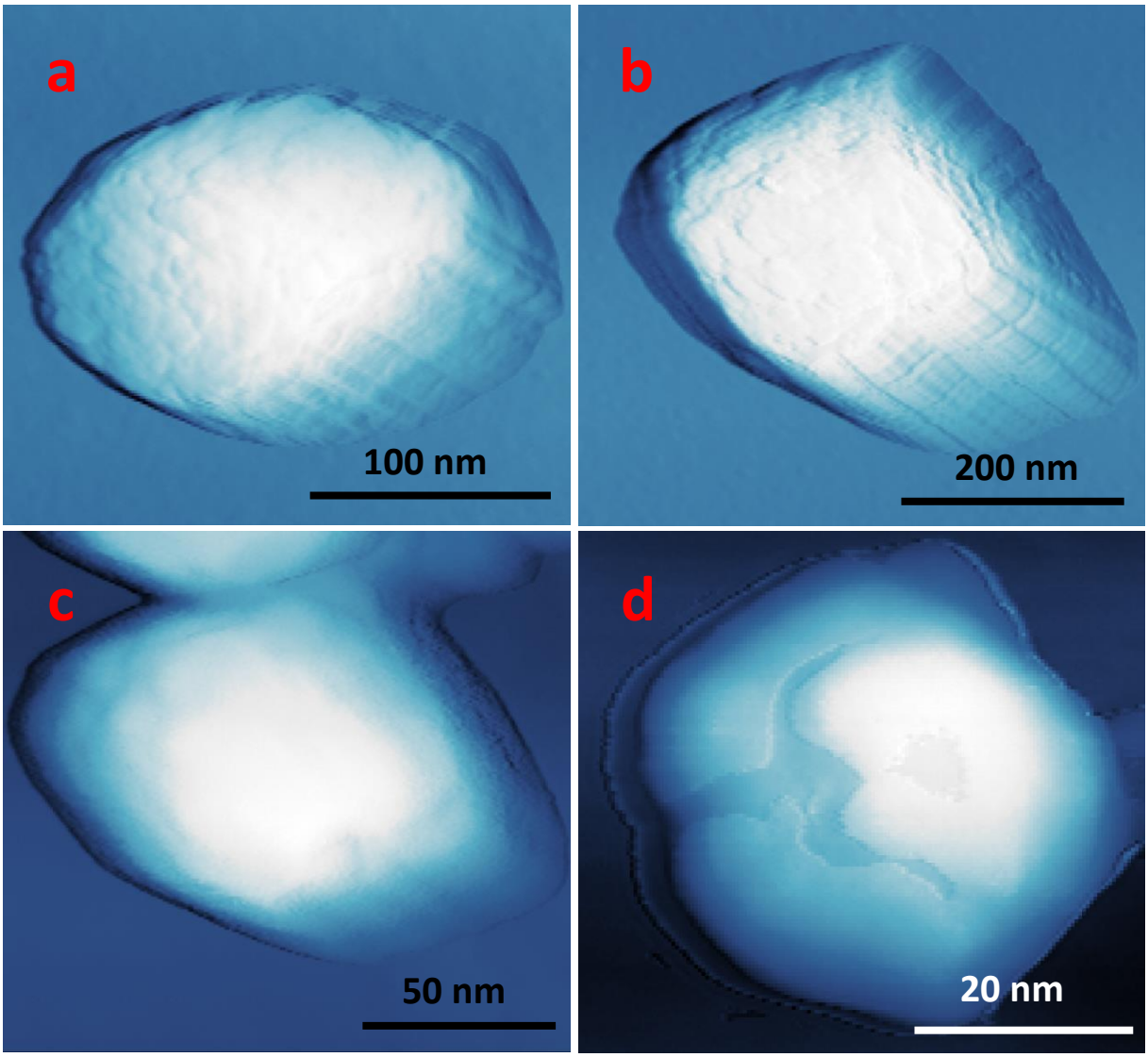

Figure S9. AFM images of the four NTP nanoparticles (final products): EG, TEG, NPA, and NBA, respectively.

Figure S9 presents the typical AFM images of the four NTP nanostructures. Accurate measurements of the heights of the NTP samples show good agreement with the size distribution statistics (Table S1). For the NTP-EG and -TEG, the AFM images (Figure S9a and b) clearly tell that both the samples are constructed from the layer-by-layer aggregation of small nanocrystals. Nevertheless, SEM images in Figure S2 show that there is always a cavity embedded in each NTP-TEG nanoparticle, suggesting a different internal arrangement during the growth process that originated from the different reaction systems. Moreover, none of the mesopores could be observed in the AFM image of the samples NTP-NPA (Figure S9c) that is totally different with the results obtained in the TEM analyses (Figure 2c). Hereafter, AFM studies of the samples NTP-NBA were also studied, and corresponding result (Figure S9d) confirms that the samples are actually made up of the self-assembly of irregular sheet-like nanostructures, which further verifies that the mesopores observed in the TEM images can be accounted for the empty cavities among the constituent fragments. On the other hand, STEM images in Figure 2c reveal that the samples NTP-NPA possess a similar construction with the samples NTP-NBA (Figure 2d). Therefore, it is reasonable to speculate that the samples NTP-NPA grow up via a similar building mode, while the main difference between them is the constituent units that possess the different sizes and morphologies. The schematic illustration of these 3D nanoarchitectures is displayed in Figure 3.

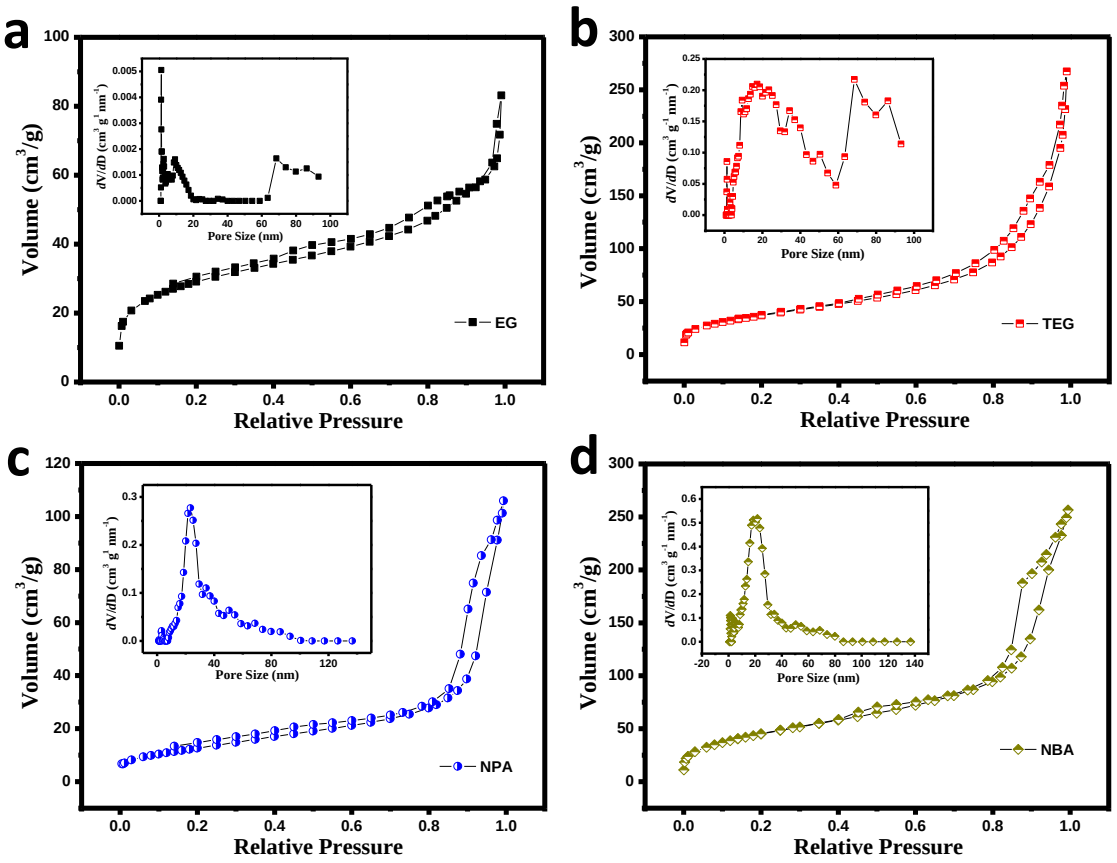

Figure S10. Nitrogen adsorption isotherms and respective pore size distributions (insets) of the four NTP nanoparticles.

Table S2. The BET surface areas and pore size distributions of the products.

	BET Surface Area (m^2/g)	Total Pore Volume (cm^3/g)	Mesopore Volume (cm^3/g)	Macropore Volume (cm^3/g)
EG	101.956	0.114	0.071	0.04
TEG	134.769	0.426	0.306	0.12
NPA	46.777	0.170	0.135	0.034
NBA	165.849	0.409	0.369	0.04

The N_2 adsorption experiments were conducted to investigate the porosity of the products (Figure S10) and corresponding results are exhibited in Table S2. The BET surface areas of the four NTP nanocubes appear to be absolutely dependent on the 3D architectures. Firstly, the samples NTP-NBA with the minimal grain sizes are constructed from the self-assembly of irregular sheet-like nanostructures which accompany by the emergence of numerous nanopores, resulting in the biggest surface areas. By contrast, the constituent nanosheets of NTP-NPA should be much larger than the samples NTP-NBA that leads to a larger particle size and the smallest surface area. Secondly, in spite of huge grain sizes, both the samples NTP-EG and -TEG demonstrate relatively large surface areas since they are made up by the layer-by-layer aggregation of tiny nanocrystals. Meanwhile, because of the ample cavities, the samples NTP-TEG exhibit the largest total pore volume and the highest proportion of macropore volume. Finally, it is worth noting the considerable proportion (90 %) of mesopore volume in the samples NTP-NBA that is favour to enhance the electrochemical performance.

Table S3. The discharge capacities collected at various current densities of the products (30 wt% super-p).

Rates / Samples	Discharge Capacities (mA h/g)					
	0.2C	0.5C	1C	2C	5C	10C
EG	91	86	81	78	74	65
TEG	98	95	90	87	80	73
NPA	95	95	92	91	88	86
NBA	110	107	106	105	104	101

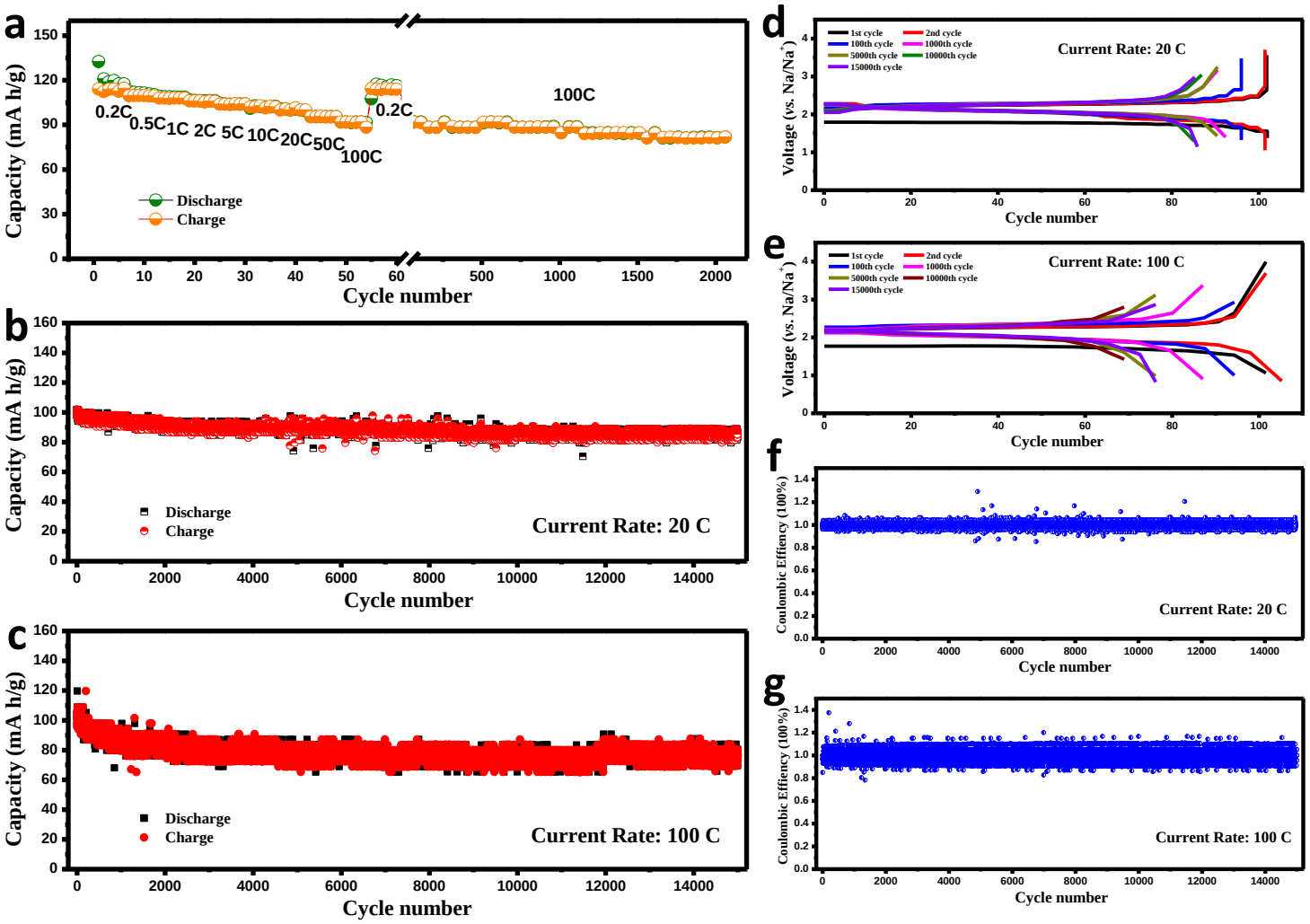

Figure S11. (a) Rate performance of the NTP-NBA nanocubes electrodes. (b, c) Reversible charge/discharge capacities against cycle number of the NTP-NBA nanocubes electrodes obtained at different current rates of 20 C and 100 C. (d, e) Corresponding charge/discharge profiles in the first, 2nd, 100th, 1000th, 5000th, 10000th and 15000th cycles of the NTP-NBA at different current rates of 20 C and 100 C. (f, g) Corresponding Coulombic efficiencies.

Figure S11 shows the rate performance of the NTP-NBA electrodes obtained at various current rates. As the current rate increased from 0.2 to 0.5, 1, 2, 5, 10 C, the discharge capacities decreased slightly from 112 to 109, 107, 105, 104 and 101 mA h/g, respectively (the errors of the delivered capacities at 0.2 and 0.5 C compared with Figure 4b in the manuscript are probably caused by the varies of the environmental temperature or the individual variability of tested batteries). At the high rate of 50 C, the delivered capacity was still ca. 95 mA h/g. Even at the extremely high rate of 100 C, ca. 81% of the initial cyclic capacity (0.2 C) was retained, suggesting the excellent high-rate performances. The NTP-NBA nanocubes electrodes have also demonstrated their superior long-term cyclic stabilities at the extremely high rates, as shown in Figure S11b and c. Nearly 85 and 76 mA h/g were retained after 15000 cycles at the 20 C and 100 C rate. Figure S11 d-g exhibit corresponding charge/discharge profiles and Coulombic efficiencies collected at high current rates of 20 C and 100 C.

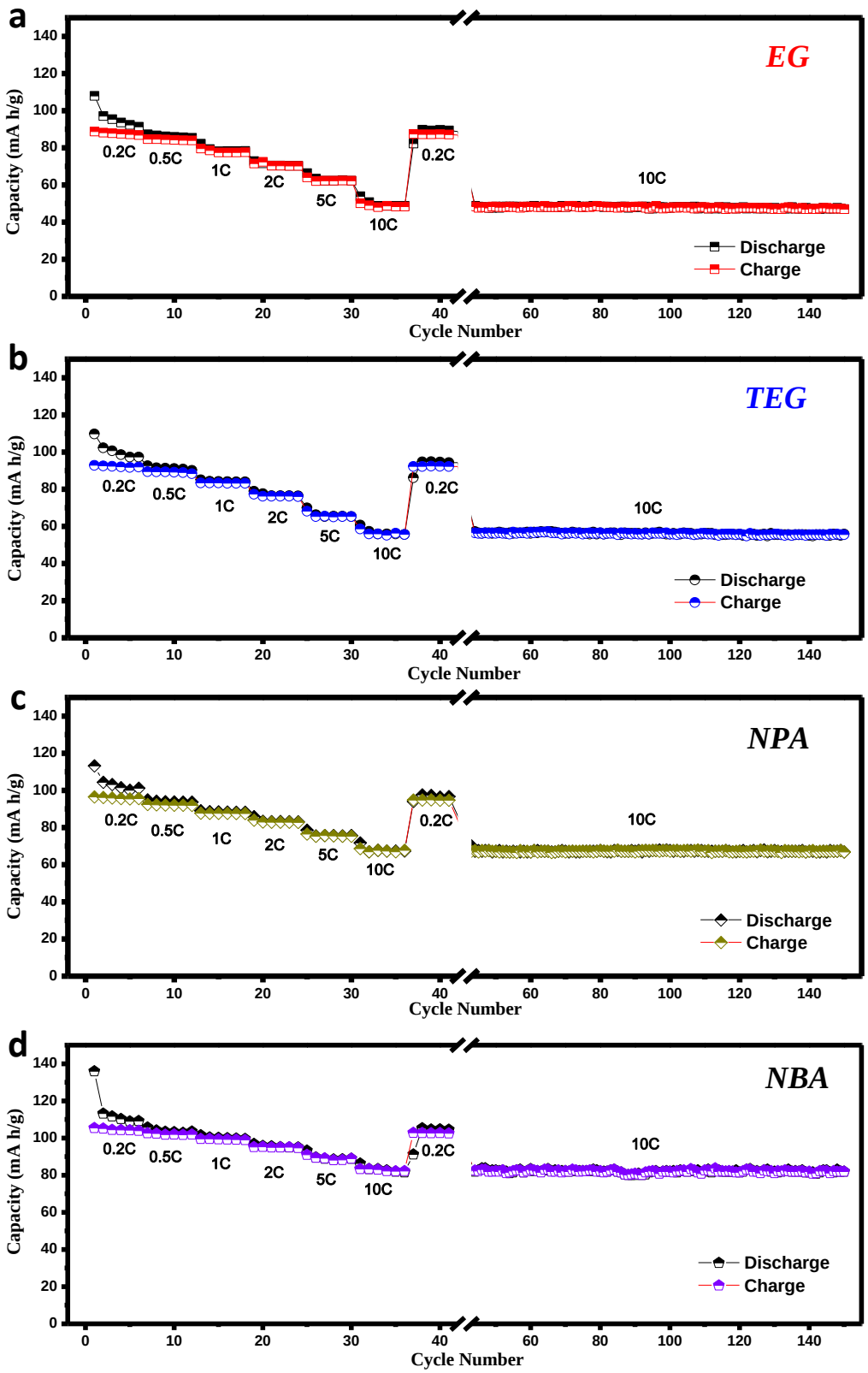

Figure S12. Rate performances of the four NTP nanocubes electrodes with 10 wt% super-p.

Table S4. The discharge capacities collected at various current densities of the four NTPs electrodes (10 wt% super-p).

Rates / Samples	Discharge Capacities (mA h/g)					
	0.2C	0.5C	1C	2C	5C	10C
EG	88	84	77	70	62	47
TEG	92	88	83	75	65	55
NPA	95	92	87	83	75	67
NBA	104	101	99	95	87	82

In order to clarify the influence of the mass percentage of carbon black, we have prepared four contrastive working electrodes which are composed of 80 wt% active material (e.g. NTP-NPA nanocubes), 10 wt% acetylene black (Super-P), and 10 wt% of sodium alginate binder (SA) with other experimental factors constant.

The electrochemical properties of the electrodes were evaluated by galvanostatic charge/discharge cycling. As can be seen in Figure S12 and Table S4, all the NTPs electrodes exhibit the comparable discharge capacities at the low current rates such as 0.2 C and 0.5 C compared with the NTPs electrodes with 30 wt% super-p (Figure 3b). However, the capacity fading tends to be faster as the rate of cycling increases. Taking the NTP-NBA nanocubes as example, the rate capacities of the electrodes remain at ca. 104 mA h/g when cycled at 0.2 C, 101 mA h/g at 0.5 C, 99 mA h/g at 1 C, 95 mA h/g at 2 C, 87 mA h/g at 5 C, and 82 mA h/g at 10 C. The delivered capacity at 10 C is only ca. 81% of the values collected from the NTPs electrodes with 30 wt% super-p. This declining capacities of high C rates probably can be attributed to the high contact resistances of the NASICON-type compounds with the intrinsic low electronic conductivity. Despite the high-rate performances are affected by the mass percentage of super-p, the capacity retentions of the NTPs electrodes with 10 wt% conductive agent are still higher than those values obtained from the best negative hosts recently tested for the sodium ion intercalation, shown in Figure S13. Moreover, all the NTP nanocubes electrodes have still demonstrated outstanding long-term cyclic stability at high rate of 10 C.

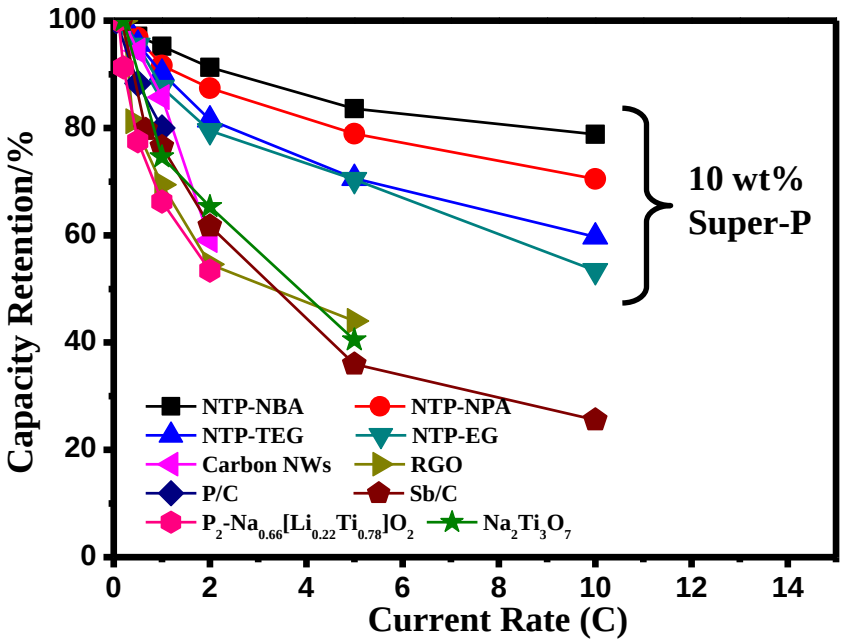

Figure S13. The capacity retention of the four NTP electrodes (10 wt% super-p) at different current rates in comparison with the best negative hosts recently tested for the sodium ion intercalation.

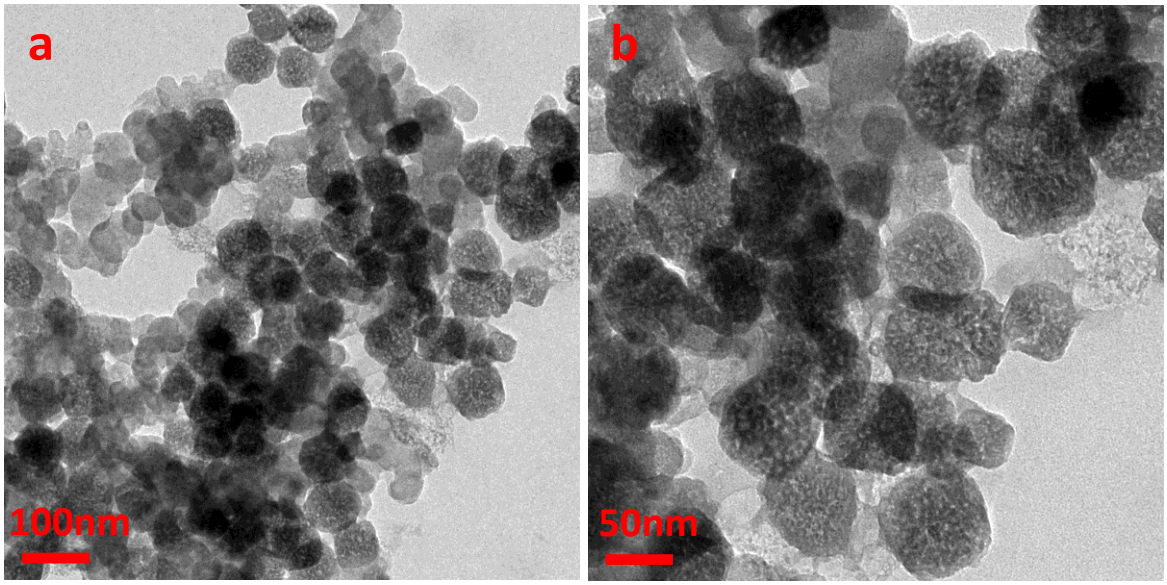

Figure S14. TEM images collected from the NTP-NBA electrodes after discharging 15000 cycles at a current rate of 100 C.